Supporting Information

Lattice Distortion of Crystalline-amorphous nickel molybdenum sulfide nanosheets for high-efficiency overall water splitting: long pair electrons' libraries and in-suit surface reconstitution

Zhikai Shi [a], *Zebin Yu** [a], *Juan Guo* [b], *Ronghua Jiang* [c], *Yanping Hou* [a], *Yushan Chen* [a], *Honglei Chen* [a], *Mi Wang* [a], *Han Pang* [a], *Wenjun Tang* [a]

[a] MOE Key Laboratory of New Processing Technology for Non-ferrous Metals and Materials, Guangxi Key Laboratory of Processing for Non-ferrous Metals and Featured Materials, School of Resources, Environment & Materials, Guangxi University, Nanning 530004, P. R. China.

[b] School of Life Sciences, Wuhan University, Wuhan, 430072, P. R. China.

[c] School of Chemical and Environmental Engineering, Shaoguan University, Shaoguan 512005, P. R. China.

Corresponding Authors:

∗ E-mail: xxzx7514@hotmail.com, yuzebin@gxu.edu.cn (Z Yu).

Tel: +8613877108420.

Content

Raman spectra of $NiMoS_4$-12/NF before and after the stability test for HER. (d) Raman spectra of $NiMoS_4$-12/NF before and after the stability test for OER. (e) EPR spectra of $NiMoS_4$-12/NF before and after the stability test for HER and OER. (f) PL spectra of $NiMoS_4$-12/NF before and after the stability test for HER and OER.

Fig. S6. SEM images of $NiMoS_4$-12/NF after the stability test for HER.

Fig. S7. SEM images of $NiMoS_4$-12/NF after the stability test for OER.

Fig. S8. (a) TEM images of $NiMoS_4$-12. (b) Strain map of $NiMoS_4$-12. FFT images of (inset of a) $NiMoS_4$-12. (c) TEM-EDX elemental mapping of $NiMoS_4$-12 after the stability test for HER.

Fig. S9. (a) TEM images of $NiMoS_4$-12. (b) Strain map of $NiMoS_4$-12. FFT images of (inset of a) $NiMoS_4$-12. (c) TEM-EDX elemental mapping of $NiMoS_4$-12 after the stability test for OER.

Fig. S10. HR-XPS spectra of (a) Ni 2p, (b) Mo 3d, and (c) S 2p of $NiMoS_4$-12/NF before and after the stability test for HER and OER. (c) HR-XPS spectra of O1s of $NiMoS_4$-12/NF before and after the stability test for OER.

Fig. S11. The ΔGH^* of $NiMoS_4$, $NiMoS_4$-Sv, and $NiMoS_4$-Sv-1 on the (104) face. The Ni, Mo, S, and H atoms are represented by Green, blue, yellow, and white spheres, respectively.

Fig. S12. A simplified diagram the in-situ Raman for $NiMoS_4$-12/NF (from OCP to 1.924 V vs. RHE).

Fig. S13. DFT simulation calculation Raman frequency of the bending and stretching vibration modes of Ni-O belonging to Ni-OOH.

Fig. S14. Structures of the reaction intermediates through the OER process on $NiMoS_4$-Sv-1 surfaces.

Fig. S15. Structures of the reaction intermediates through the OER process on Ni-OOH surfaces.

Table S1. Comparison of the element mass percentage and atomic percentage for Ni_3S_2, $NiMoS_4$-12, $NiMoS_4$-12 (HER for 100h), and $NiMoS_4$-12 (OER for 100h) from the TME-EDS.

Table S2. Comparison of electrochemical performances of HER, OER, and OWS of $NiMoS_4$-12 with recently reported top tier metal based inorganic electrocatalysts in 1 M KOH.

Physical characterization

The crystalline phases of various electrodes were analyzed by Xray diffraction (XRD) using a diffractometer (DX-2700A, Dandong, China) with Cu Ka radiation and an accelerating voltage of 40 kV in the 2θ range of 10–90°, at a scanning rate of 15° min^{-1}. Raman spectra were recorded via a Raman spectrometer (inVia Reflex, Renishaw, England) with 532 nm excitation to explore the molecular vibration and rotation information on the electrode surface. Electron paramagnetic resonance (EPR) spectra were collected at 298 K over an electron paramagnetic resonance spectrometer (Bruker A300, Bruker, German) to measure defect species. Photoluminescence (PL) spectra was obtained via a steady-state fluorescence spectrum analyzer (OmniFluo-960, ZOLIX, China) with an excitation wavelength of 532 nm.

The electrode surface morphologies were characterized by a field-emission scanning electron microscopy (FESEM, Hitachi SU8020, Japan). High-resolution transmission electron microscopy (HR-TEM) was carried out to characterize the inner structures of the catalysts using a FEI TECNAI G2 F30 instrument from USA at 300 kV, and the elemental compositions of the electrodes were investigated by an energy-dispersive X-ray spectroscopy (EDS). The electrode samples were ultrasonically dispersed in ethanol, and the testing samples were prepared by dropping the dispersed suspensions onto the carbon film-coated copper meshes.

X-ray photoelectron spectroscopy (XPS) was performed to gain insight into the chemical composition and binding states of the electrodes on a Thermo Scientific K-Alpha (USA) instrument with a monochromatic Al Ka X-ray source.

Nitrogen adsorption-desorption isotherms were applied to examine the specific surface areas and the pore size distribution via the Brunauer–Emmett–Teller (BET; ASAP2460, America) and Barrett–Joyner–Halenda (BJH) methods at 57.3 K.

Electrochemical measurements

All electrochemical measurements were conducted using an electrochemical workstation (CHI 660E, China) using a typical three-electrode system in a quartz electrolytic cell, with the prepared catalyst materials as the working electrode, a graphite rod electrode as the counter electrode, a $Hg|HgO|OH^-$ electrode as the reference electrode, and the 1 M KOH solution as the electrolyte at room temperature. Before the electrochemical tests, the electrolyte was purged with N_2 for 30 min to remove O_2. The potential values in this study were converted and referred to the reversible hydrogen electrode (RHE) using the Nernst equation, $E(RHE)= E (vs. Hg|HgO|OH^-) + 0.059*pH + 0.098 V= E (vs. Hg|HgO|OH^-) + 0.924 V$. The overpotential ($\eta$) was calculated by using the equation: $\eta = E(RHE) - 1.23$ V for the OER. Linear sweep voltammetry (LSV) polarization curves for the HER and OER were conducted at a scan rate of 5 mV s^{-1} with 95% iR compensation. The durability was tested at current densities of 100 mA cm^{-2} for 100 h for the HER and OER. Electrochemical impedance spectroscopy (EIS) was performed within the frequency range of 100 kHz to 0.01 Hz with an AC potential

amplitude of 5 mV at open circuit voltage for the HER and OER. The electrochemically active surface areas (ECSAs) of the electrodes were characterized by conducting cyclic voltammetry (CV) with various scan rates of 20, 40, 60, 80, and 100 mV s^{-1} in the non-Faradiac region within the potential range from 0.124 V to 0.324 V (vs. RHE). The ECSAs value is equal to the ratio of the dual-layer capacitances (Cdl) of the substance to the normally accepted reference specific capacitance (Cs= 0.040 mF cm^{-2}).

Density functional theory (DFT) calculations

The density of states of $NiMoS_4$, $NiMoS_4$-Sv, and $NiMoS_4$-Sv-1 were studied using the electronic structure obtained from the periodic DFT calculations performed through the CASTEP code. Generalized gradient approximation (GGA) for the exchange-correlation using Perdew, Burke and Emzerhof (PBE) was employed to examine the electronic structure for all the above structure. For this simulation, the Quality, the Energy cutoff and the k-point were set as fine, 421.80 eV and (4×4×4 $Å^{-1}$), respectively.

In-situ Raman experiments

A specially made Teflon based electrochemical cell was used for the combined electrochemical and in situ Raman spectroscopy study. This cell contains a Pt wire and a $Hg|HgO|OH^-$ electrode, served as a counter electrode and reference electrode, respectively. The $NiMoS_4$-12/NF electrode was used as a working electrode. In situ Raman spectra of the sample electrodes were recorded using a confocal Raman microscope (Hitachi High-tech SU8020). The laser beam (532 nm, green) was focused

through a microscope objective (×50) onto a circular area of 1 mm in diameter on the $NiMoS_4$-12/NF electrode and the backscattered light was collected through the same objective. The in-situ Raman experiments were conducted to exploring electrode surface changes at an increasing applied voltage from 1.524 to 1.924 V vs. RHE in 1 M KOH by using green (532 nm) excitation laser lines.

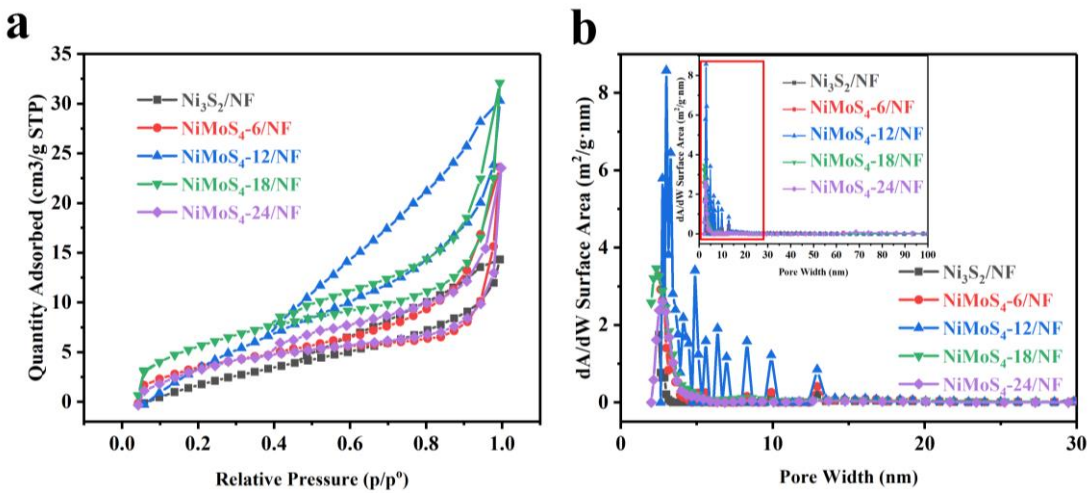

Fig. S1. (a) N_2 adsorption/desorption isotherms of Ni_3S_2/NF, $NiMoS_4$-6/NF, $NiMoS_4$-12/NF, $NiMoS_4$-18/NF, and $NiMoS_4$-24/NF, respectively. (b) The pore size distribution of Ni_3S_2/NF, $NiMoS_4$-6/NF, $NiMoS_4$-12/NF, $NiMoS_4$-18/NF, and $NiMoS_4$-24/NF, respectively.

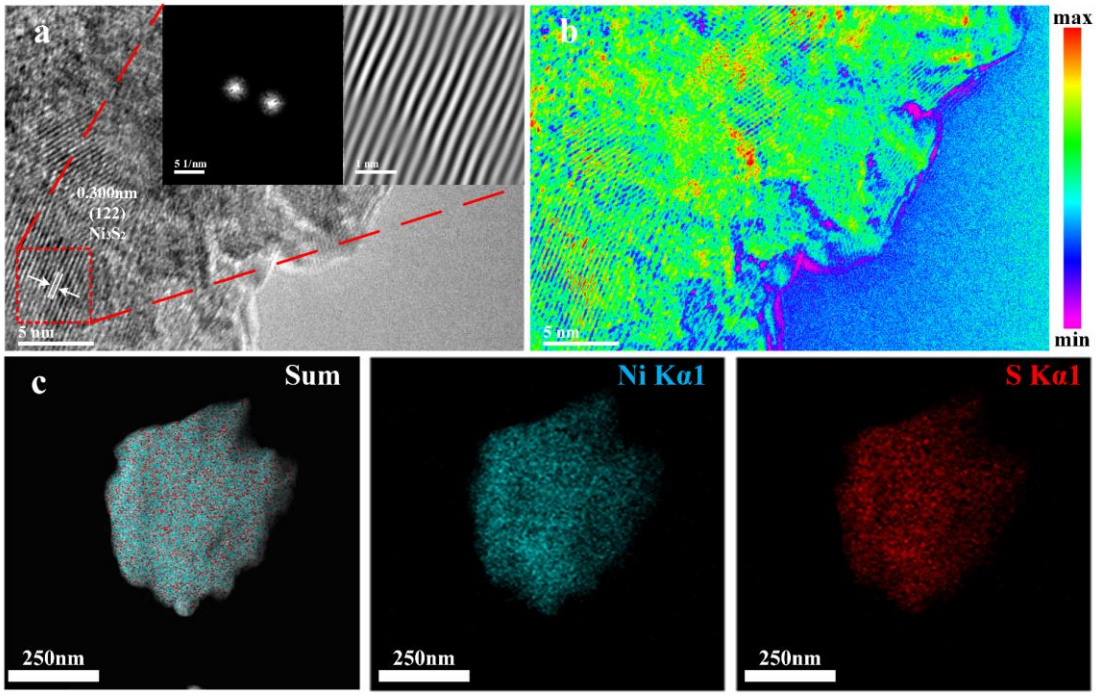

Fig. S2. (a) TEM images of Ni_3S_2. (b) Strain map of Ni_3S_2. FFT images of (inset of a) Ni_3S_2. (c) TEM-EDX elemental mapping of Ni_3S_2.

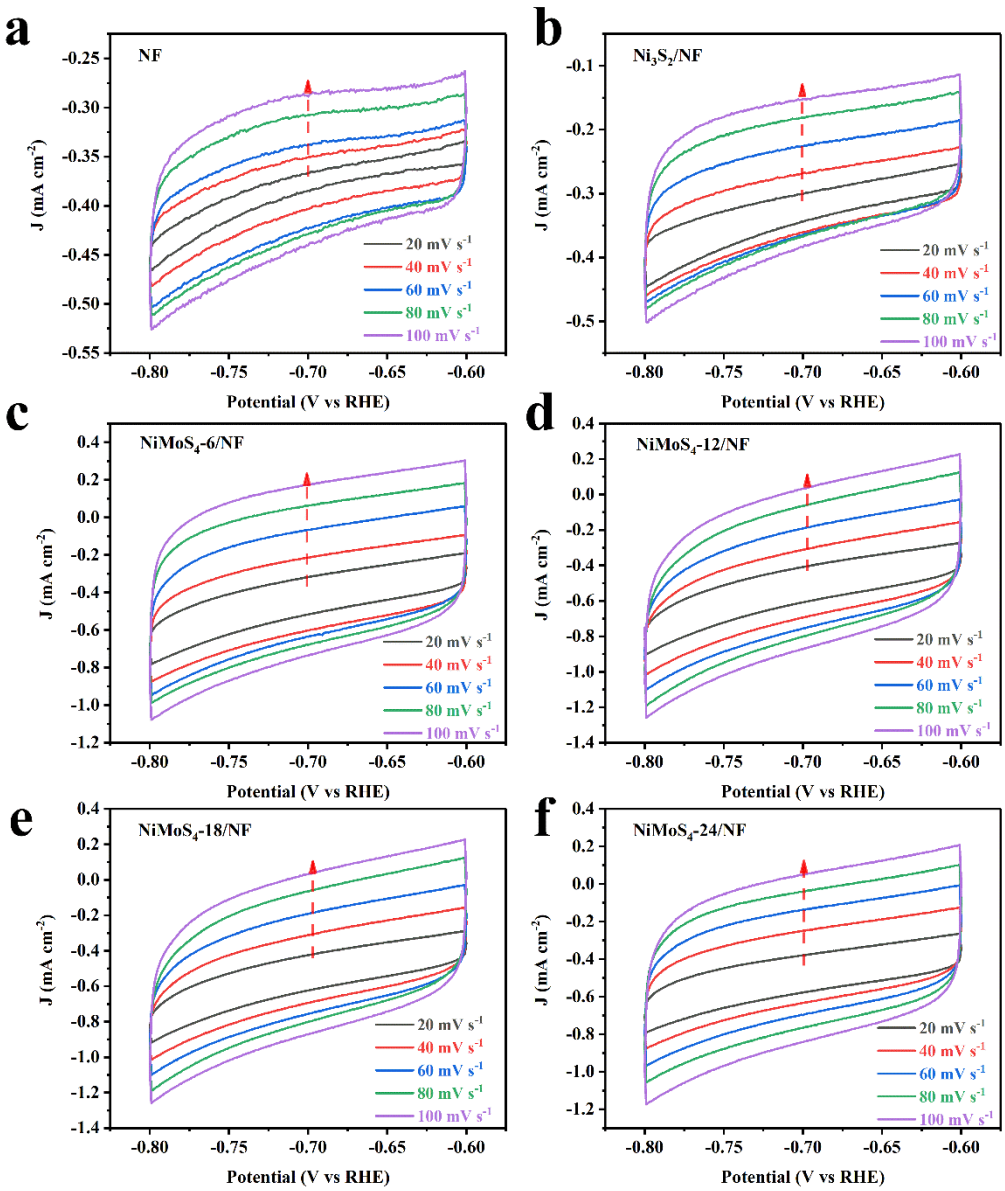

Fig. S3. CV curves of (a) NF, (b) Ni_3S_2/NF, (c) $NiMoS_4$-6/NF, (d) $NiMoS_4$-12/NF, (e) $NiMoS_4$-18/NF, and (f) $NiMoS_4$-24/NF at increasing scan rates from 20 mV s^{-1} to 100 mV s^{-1}.

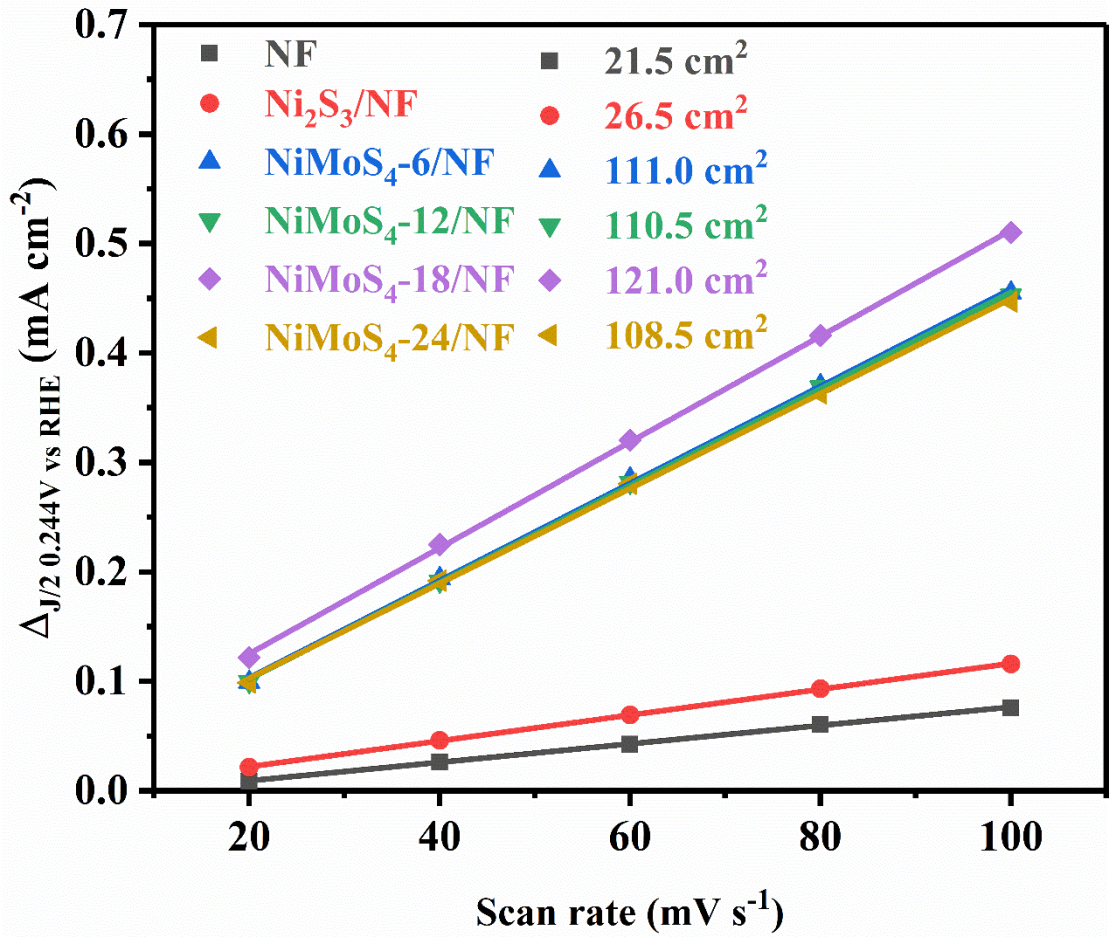

Fig. S4. Plots used for evaluating the ECSA of NF, Ni_3S_2/NF, $NiMoS_4$-6/NF, $NiMoS_4$-12/NF, $NiMoS_4$-18/NF, and $NiMoS_4$-24/NF as a function of scan rate.

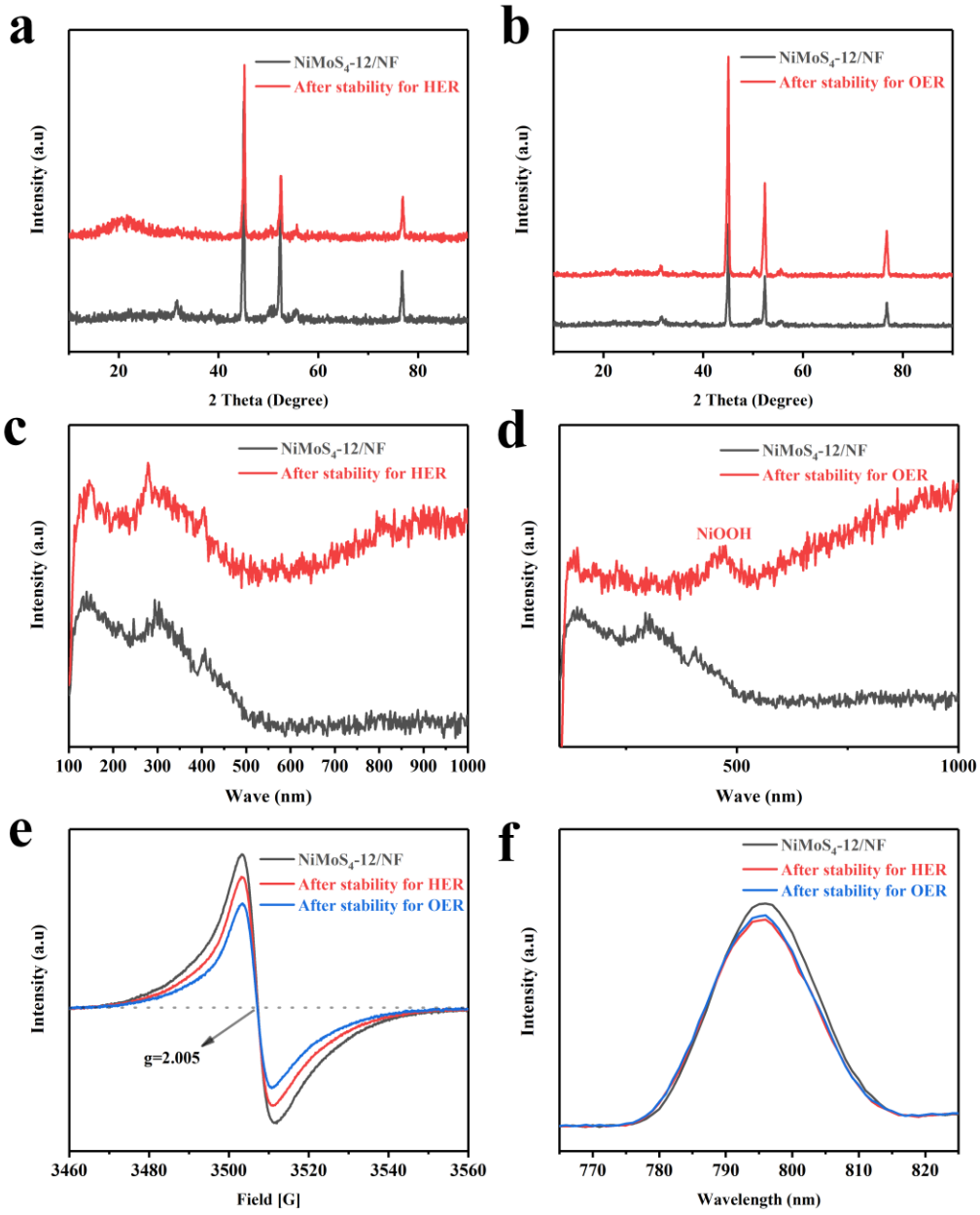

Fig. S5. (a) XRD patterns of $NiMoS_4$-12/NF before and after the stability test for HER. (b) XRD patterns of $NiMoS_4$-12/NF before and after the stability test for OER. (c) Raman spectra of $NiMoS_4$-12/NF before and after the stability test for HER. (d) Raman spectra of $NiMoS_4$-12/NF before and after the stability test for OER. (e) EPR spectra of $NiMoS_4$-12/NF before and after the stability test for HER and OER. (f) PL spectra of $NiMoS_4$-12/NF before and after the stability test for HER and OER.

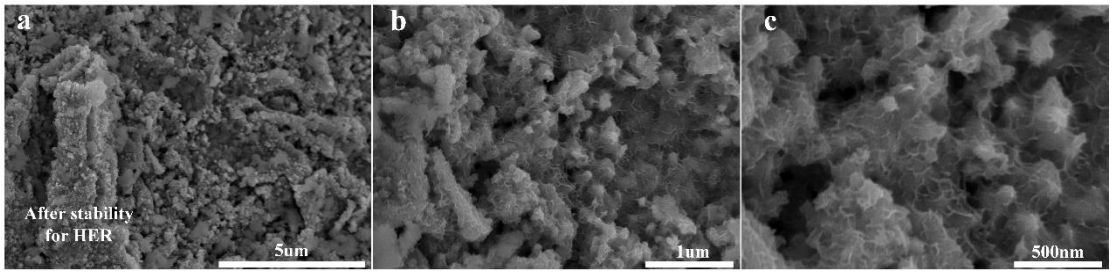

Figure S6. SEM images of $NiMoS_4$-12/NF after the stability test for HER.

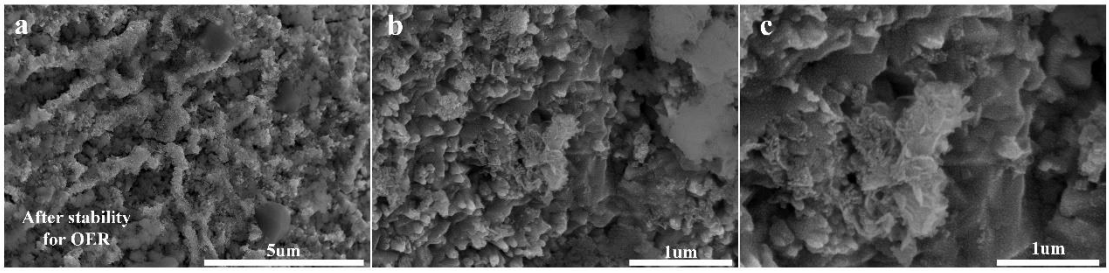

Fig. S7. SEM images of $NiMoS_4$-12/NF after the stability test for OER.

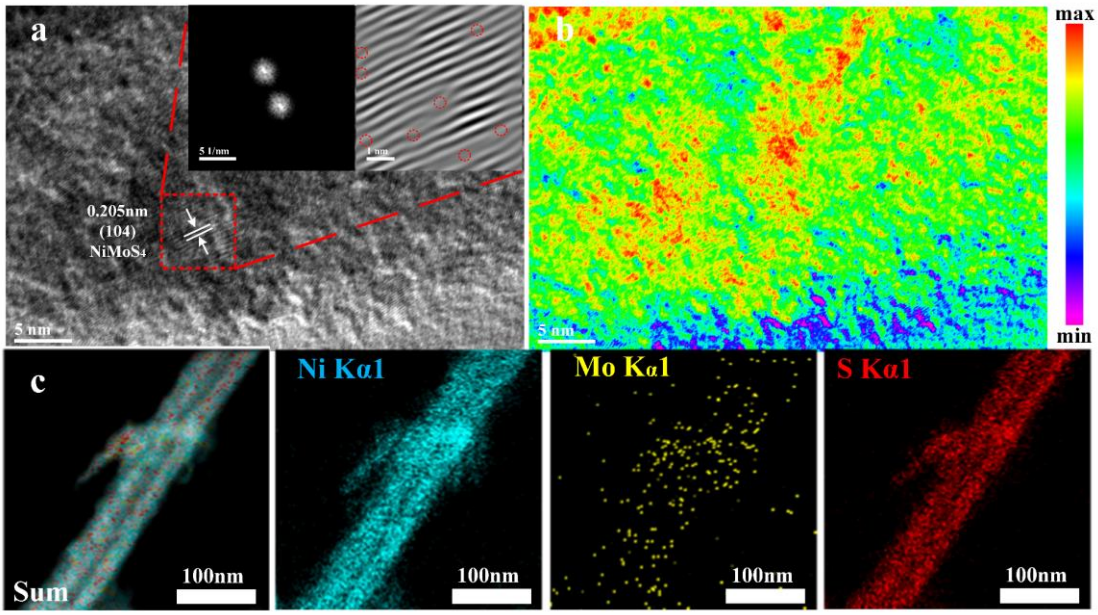

Fig. S8. (a) TEM images of $NiMoS_4$-12. (b) Strain map of $NiMoS_4$-12. FFT images of (inset of a) $NiMoS_4$-12. (c) TEM-EDX elemental mapping of $NiMoS_4$-12 after the stability test for HER.

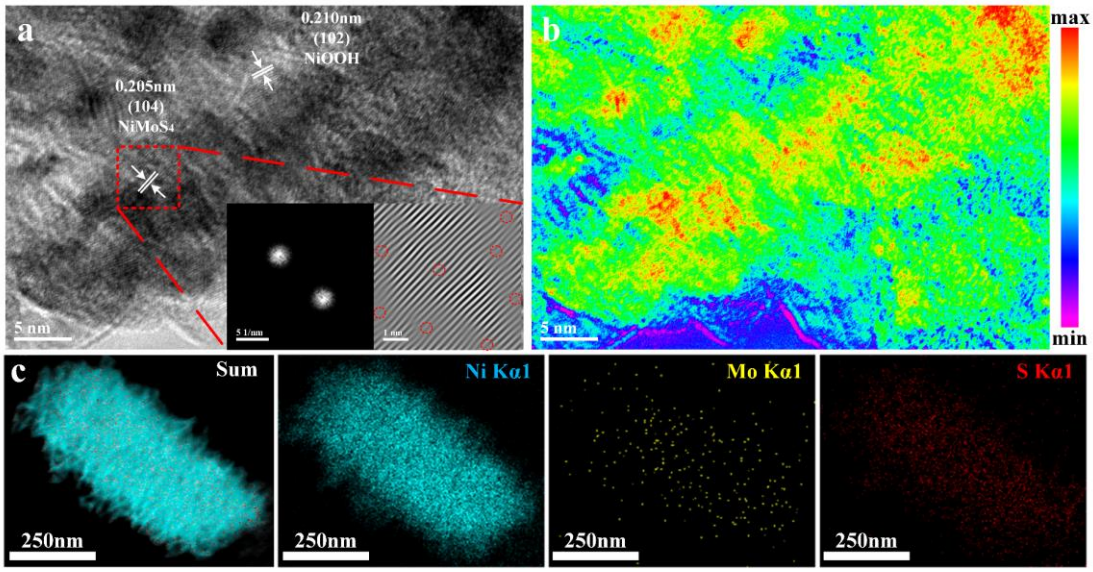

Fig. S9. (a) TEM images of $NiMoS_4$-12. (b) Strain map of $NiMoS_4$-12. FFT images of (inset of a) $NiMoS_4$-12. (c) TEM-EDX elemental mapping of $NiMoS_4$-12 after the stability test for OER.

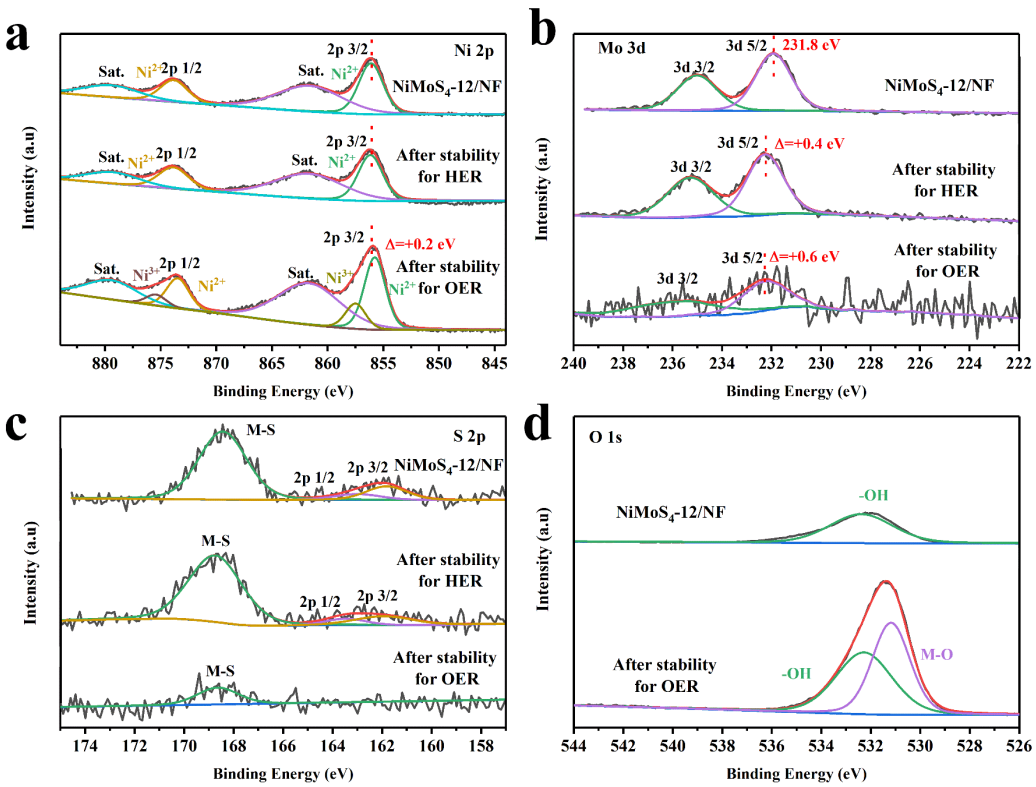

Fig. S10. HR-XPS spectra of (a) Ni 2p, (b) Mo 3d, and (c) S 2p of $NiMoS_4$-12/NF before and after the stability test for HER and OER. (c) HR-XPS spectra of O1s of $NiMoS_4$-12/NF before and after the stability test for OER.

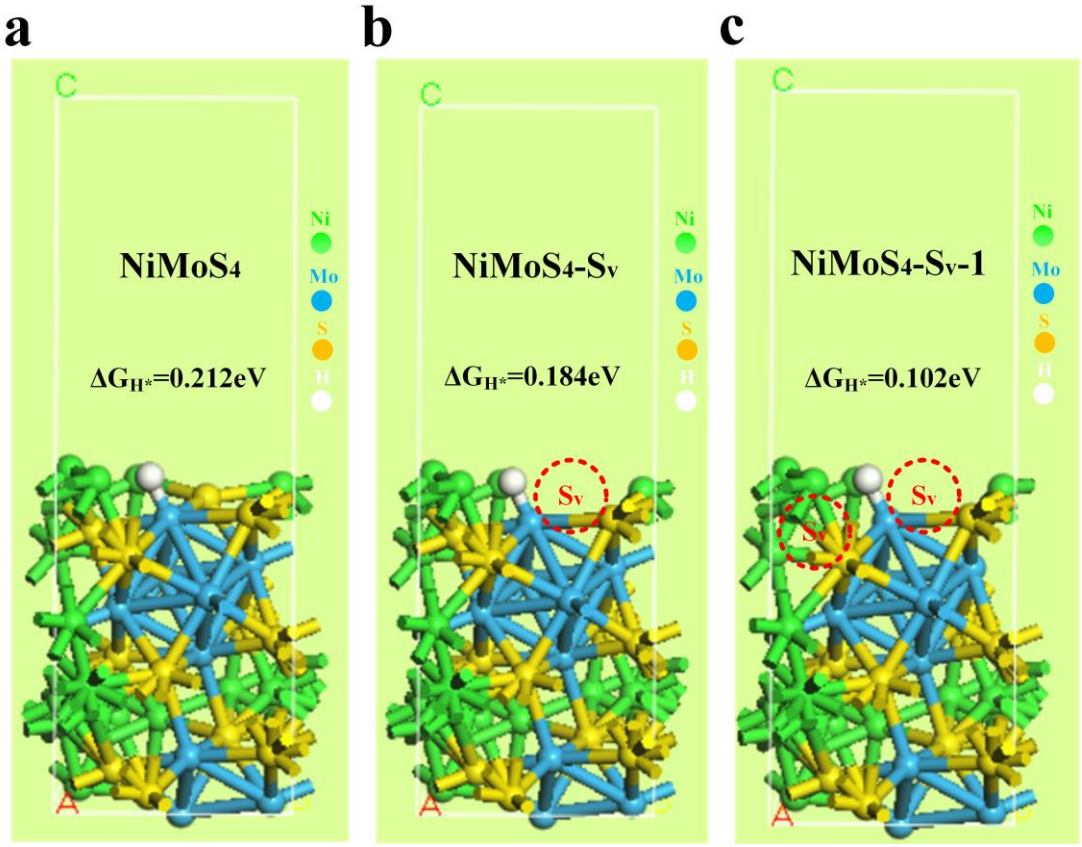

Fig. S11. The ΔG_{H^*} of $NiMoS_4$, $NiMoS_4$-Sv, and $NiMoS_4$-Sv-1 on the (104) face. The Ni, Mo, S, and H atoms are represented by Green, blue, yellow, and white spheres, respectively.

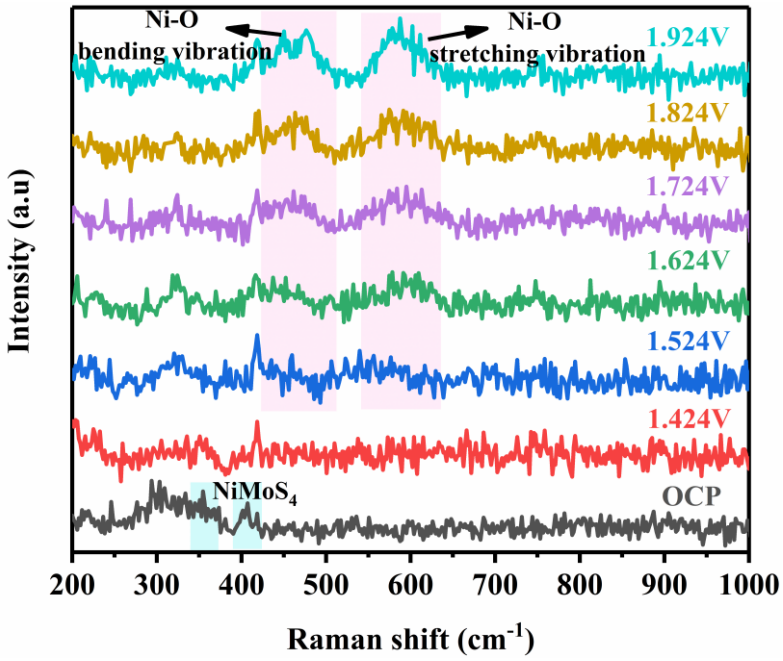

Fig. S12. A simplified diagram the in-situ Raman for $NiMoS_4$-12/NF (from OCP to 1.924 V vs. RHE).

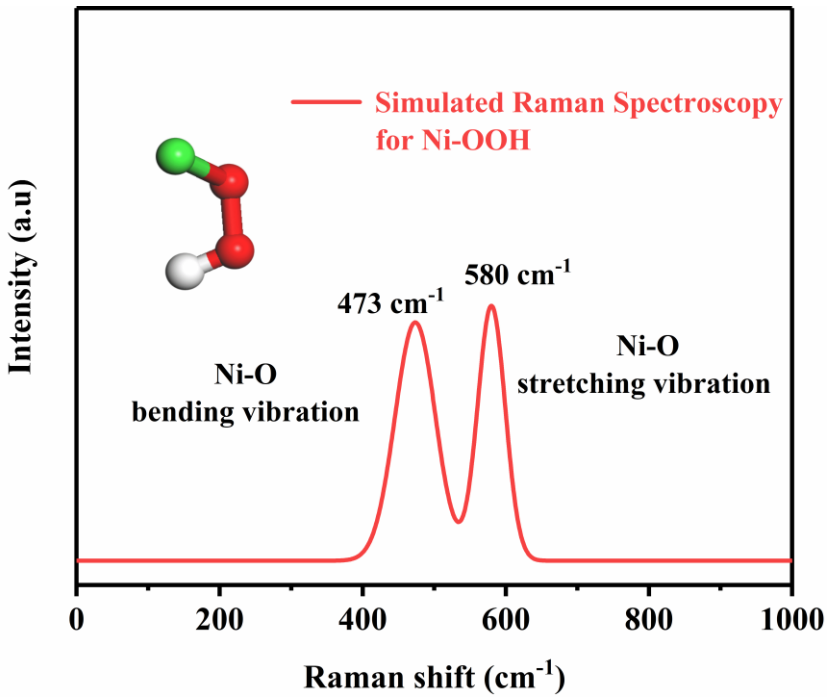

Fig. S13. DFT simulation calculation Raman frequency of the bending and stretching vibration modes of Ni-O belonging to Ni-OOH.

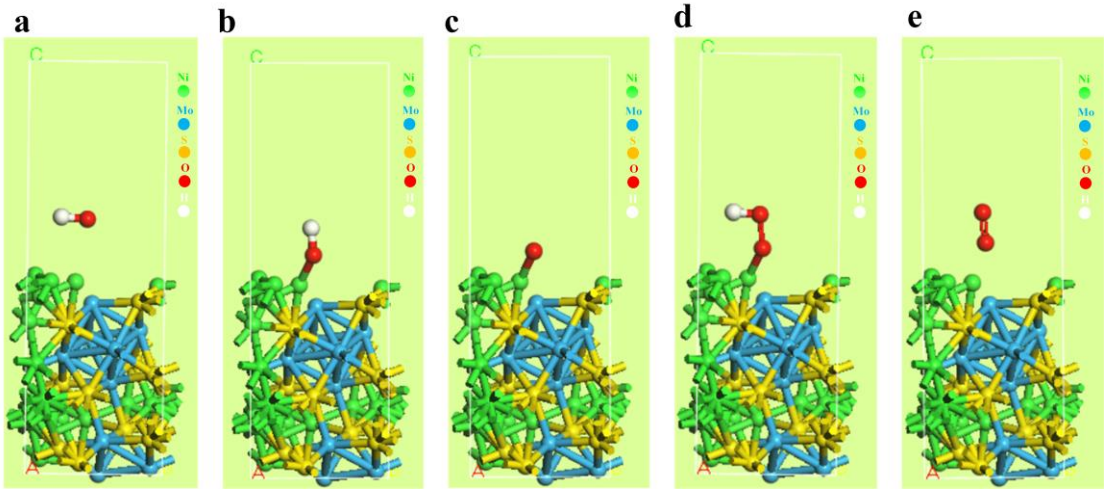

Fig. S14. Structures of the reaction intermediates through the OER process on $NiMoS_4$-Sv-1 surfaces.

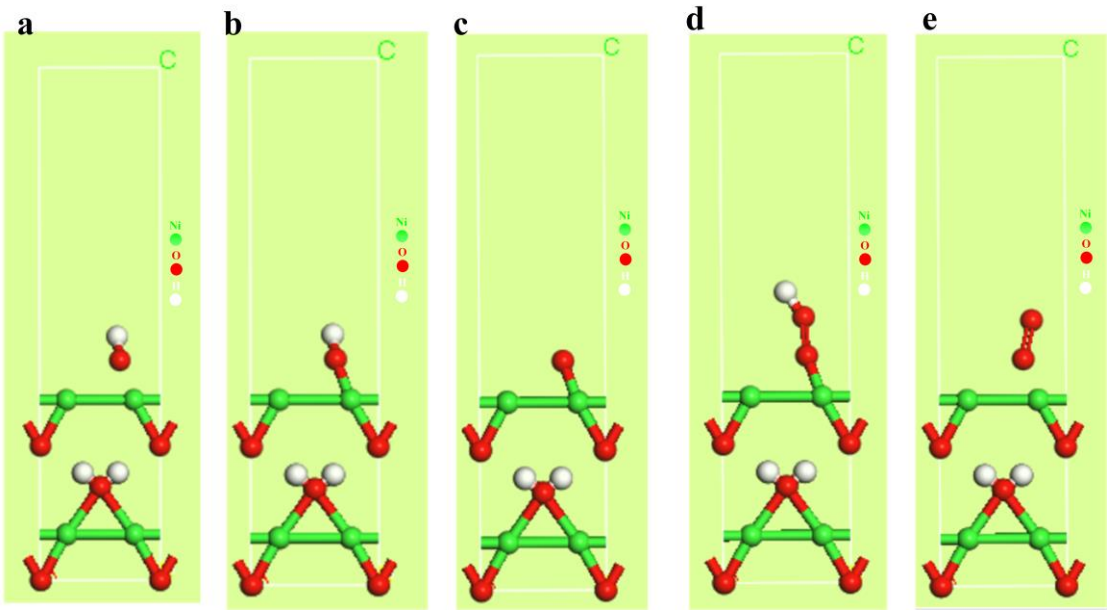

Fig. S15. Structures of the reaction intermediates through the OER process on Ni-OOH surfaces.

Table S1. Comparison of the element mass percentage and atomic percentage for Ni_3S_2, $NiMoS_4$-12, $NiMoS_4$-12 (HER for 100h), and $NiMoS_4$-12 (OER for 100h) from the TME-EDS.

Catalysts	Element	wt%	Atomic percentage
Ni_3S_2	S	27.93	41.5
	Ni	72.07	58.5
$NiMoS_4$-12	S	42.29	62.97
	Ni	26.33	21.42
	Mo	31.38	15.61
HER for 100h	S	35.66	55.17
	Ni	35.26	29.8
	Mo	29.08	15.03
OER for 100h	O	1.72	5.21
	S	33.59	50.89
	Ni	34.72	28.73
	Mo	29.97	15.17

Table S2. Comparison of electrochemical performances of HER, OER, and OWS of $NiMoS_4$-12 with recently reported top tier metal based inorganic electrocatalysts in 1 M KOH.

Catalysts	HER	OER	OWS	Ref.
	η_{10} (mV)	η_{10} (mV)	η_{10} (V)	
$NiMoS_4$-12	**119**	**273**	**1.47**	**This work**
MoS_2-NiS_2/N-doped graphene	172	370	1.64	[1]
NiCoFeP/C	149	270	1.60	[2]
Ni_3S_2@NGCLs/NF	134	271	1.55	[3]
CoP@FeCoP/NC YSMPs	141	238	1.68	[4]
$CoSe_2$@MoSe	183	309	1.52	[5]
Carbon-incorporated NiO/Co_3O_4	169.5	290	1.63	[6]
Ni–Fe–P nanocubes	182	271	1.67	[7]
NiCoFeP	131	273	-	[8]
NiFe-NC	197	271	1.67	[9]

References

1. P. Kuang, M. He, H. Zou, J. Yu and K. Fan, *Applied Catalysis B: Environmental*, 2019, **254**, 15-25.
2. X. Wei, Y. Zhang, H. He, L. Peng, S. Xiao, S. Yao and P. Xiao, *Chemical Communications*, 2019, **55**, 10896-10899.
3. B. Li, Z. Li, Q. Pang and J. Z. Zhang, *Chemical Engineering Journal*, 2020, **401**, 126045.
4. J. Shi, F. Qiu, W. Yuan, M. Guo and Z.-H. Lu, *Chemical Engineering Journal*, 2021, **403**, 126312.
5. Z. Chen, W. Wang, S. Huang, P. Ning, Y. Wu, C. Gao, T.-T. Le, J. Zai, Y. Jiang, Z. Hu and X. Qian, *Nanoscale*, 2020, **12**, 326-335.
6. X. Wei, Y. Zhang, H. He, D. Gao, J. Hu, H. Peng, L. Peng, S. Xiao and P. Xiao, *Chemical Communications*, 2019, **55**, 6515-6518.
7. C. Xuan, J. Wang, W. Xia, Z. Peng, Z. Wu, W. Lei, K. Xia, H. L. Xin and D. Wang, *ACS Appl. Mater. Interfaces*, 2017, **9**, 26134-26142.
8. Y. Guo, J. Tang, Z. Wang, Y. Sugahara and Y. Yamauchi, *Small*, 2018, **14**, 1802442.
9. A. Kumar and S. Bhattacharyya, *ACS Appl. Mater. Interfaces*, 2017, **9**, 41906-41915.